



Experimental study of force, pressure, and fluid velocity on a simplified coastal building under tsunami bore impact

Wei-Liang Chuang^{1,2} · Kuang-An Chang^{1,3}  · James Kaihatu¹ · Rodrigo Cienfuegos^{4,5} · Cyril Mokrani⁴

Received: 29 July 2019 / Accepted: 25 April 2020 / Published online: 11 May 2020
© Springer Nature B.V. 2020

Abstract

The present study experimentally investigated the flow kinematics and hydrodynamic pressures and forces on a simplified coastal building under tsunami bore impact. A rectangular structure sitting on a 1/10 sloping beach at four different headings, at 0°, 15°, 30° and 45°, was considered under bore impacts. The input wave condition was designed to generate a tsunami bore traveling at high speed on a sloping beach. The interaction between bore and structure (oriented at four different headings) was investigated using the nonintrusive bubble image velocimetry technique that enables the quantitative visualization of the full-field flow behavior. Simultaneous measurements of forces and pressures during the impacts were correlated with the measured flow velocities. As the tsunami bore is highly turbulent, ensemble averages from repeated tests were obtained for the investigation. To model the interaction, the validity of a dam break solution for a sloping bed as a suitable representation was examined, while the initial water depth was approximated using wave properties and calibrated with measured bore celerity. The study found that the profile of peak impact pressures is similar to a hydrostatic distribution for each heading, but one order of magnitude greater than the hydrostatic pressure. Similar linear distribution is also found in the correlation between peak impact pressure and angle of heading. By correlating the peak impact pressures with the impact velocity, the impact coefficient was estimated as 0.55. The measured pressures were further applied to model the surge force. By examining the peak surge forces against the heading angle, the lowest magnitude occurred when the structure was orientated at 30°.

Keywords Tsunami bore · Tsunami force · Bore impact · Dam break model · Particle image velocimetry

✉ Kuang-An Chang
kchang@tamu.edu

Extended author information available on the last page of the article

1 Introduction

Tsunamis are very long waves traveling in the ocean, mostly generated as a consequence of geophysical forces such as earthquakes, submarine landslides, and volcanic eruptions. The extensive casualties and destructions to the coastal communities during the 2004 Indian Ocean and 2011 Tohoku tsunamis have raised public awareness of the hazards. Examinations on the appropriateness of existing designs to mitigate the hazards and evaluate the inundations and impact forces have also been performed. Regarding structure integrity, several post-tsunami surveys for the 2004 Indian Ocean Tsunami (Fritz et al. 2006; Ghorbarah et al. 2006; Tomita et al. 2006) and the 2011 Tohoku Tsunami (Shimozono et al. 2012; Liu et al. 2013) reported damages to inland structures such as transportation facilities, coastal defense systems, and houses. Those surveys provide essential information for further investigations on the interaction between tsunami waves and coastal structures to improve structure design and survivability.

St-Germain et al. (2014) addressed four types of tsunami inland intrusions categorized by Takahashi et al. (2011) from the 2011 Tohoku Tsunami post-survey: *overtopping*, *breaking wave*, *slowly varying*, and *high run-up*. According to St-Germain et al., the *overtopping* type occurs in port area when tsunami wave overtops the quay wall without breaking; very high flow velocities would accompany in such scenario. The *breaking wave* type features the scenario similar to a surging breaker in which a tsunami wave breaks at or close to a shoreline and runs up onto a mild-slope beach. The run-up in the form of a bore can reach up to several kilometers inland over low-lying landscape. The *slowly varying* type emerges when a tsunami wave encounters a steep cliff in deep water and bounces back with a relatively smooth up-and-down motion. The *high run-up* type is characterized as a tsunami wave breaking inland on a relatively steep-slope beach and reaching a significant run-up height at a high speed. Based on the literature, many studies investigated impacts on structures under tsunami bores caused by the breaking wave type (e.g., Robertson et al. 2011, 2013; Chinnarasri et al. 2013; Linton et al. 2013; Moon et al. 2014; Rahman et al. 2014; Kihara et al. 2015; Shafiei et al. 2016). However, research on the more destructive overtopping and high run-up types is relatively limited. In particular, the high run-up type can be a greater threat to a densely populated area. This motivates the present study to consider the high run-up type tsunami bore impacts.

Numerous laboratory studies have been performed to improve our understanding on the interactions between tsunami waves and coastal structures for the breaking wave intrusion type. Some studies focused on tsunami bore impacts on vertical walls in flumes (Cross, 1967; Linton et al. 2013; Robertson et al. 2011, 2013; Kihara et al. 2015), while others concentrated on low-crested coastal structures that allow wave overtopping to occur during tsunami bore impacts (Asakura et al. 2000; Thusyanthan and Madabhushi 2008; Fujima et al. 2009; Chinnarasri et al. 2013; Moon et al. 2014; Rahman et al. 2014). In addition, Palermo et al. (2012) considered square and circular cylinders with a height that prevents overtopping from occurring. Their work examined the 3-D effects of the tsunami impact and identified impulsive, run-up, and quasi-steady hydrodynamic signatures from force time histories. Yeh (2007) examined vertical forces and identified impulsive, hydrodynamic drag, hydrodynamic lift, and buoyant forces during tsunami impacts. Cawley (2014) pointed out the need of investigating tsunami loadings to different building shapes and orientations. Inspired by Cawley's study, Shafiei et al. (2016) performed a comprehensive experimental investigation of tsunami bore impacts on a square prism with six different orientations. They examined the relation between bore heights and bore velocities and

numerically modeled the streamwise (surge) and upward maximum forces and reported relevant drag coefficients at each heading.

In addition to forces, it is been commonly agreed that high pressures induced by tsunami bore impacts could lead to local damage that may deteriorate structural integrity and result in structure failure. Palermo et al. (2012) suggested that hydrostatic pressure may be used to approximate pressure distributions on the upstream face of a square structure. On the contrary, both Nouri et al. (2010) and Kihara et al. (2015) identified two types of pressures exerted during tsunami impact: (a) an impulsive pressure with a short duration of $O(\text{ms})$ and (b) a quasi-steady pressure with a longer duration of $O(\text{s})$. The quasi-steady pressure is associated with the hydrostatic pressure, while the impulsive pressure is similar to the mechanisms in breaking wave impacts (Bagnold 1939; Peregrine 2003) that often result in a high pressure magnitude with a very short duration. On the other hand, surge forces may be estimated using measured impact pressures. Shafiei et al. (2016) successfully calculated the time history of surge forces using measured pressures with the assumption of a uniform pressure distribution over the structure width at six different orientations. In addition, Robertson et al. (2011, 2013) suggested that considering the additional loading exerted by the reverse flow is needed to accurately estimate the peak surge forces using peak impact pressures.

To determine the hydrodynamic pressures or forces acting on a structural wall, it is crucial to know the tsunami velocities prior to the impact. Kihara et al. (2015) determined that the ideal flow model of Ritter (1892) can be used to describe the tsunami bore velocity profile along its propagation. However, Shafiei et al. (2016) showed that the front region of the bore is better described by a real fluid model with the friction slope taken into account (Chanson 2006). The dam break models proposed by Ritter (1892) and Chanson (2006) provide simple formulas to estimate the bore front velocity (U_B). However, the one-dimensional flow assumption limits their applications to realistic tsunami–structure interactions in which the flows are three-dimensional. Even though the bore velocity may be estimated by the bore height, researchers (e.g., Murty 1977; Kirkoz 1983; Bryant 2001; Matsutomi and Okamoto 2010; Shafiei et al. 2016) have shown that the empirical coefficients used in the estimation are affected by the Froude number of the bore. Palermo et al. (2012) concluded that a proper assessment of momentum flux is needed to accurately predict the time history of hydrodynamic pressures and forces. To achieve that, advanced approaches or measurement techniques are desired to determine the time-varying, full-field velocities in two-dimensional or three-dimensional sense.

To the authors' knowledge, no nonintrusive velocity measurements that quantify the interaction between tsunami bore and structure heading have been reported, even though such information is crucial in understanding the resulting pressures and forces. The major challenge lies on the highly aerated and turbulent nature in tsunami bores that hampers the use of the traditional particle image velocimetry (PIV) technique to quantify its flow field (Kihara et al. 2015). Alternatively, Ryu et al. (2005) introduced bubble image velocimetry (BIV), a derivative from PIV, to measure flow velocities in aerated turbulent flows, such as sloshing, green water, and breaking waves. Unlike PIV in which seeding particles are illuminated by high-energy laser, BIV requires only a simple backlit light source to enhance the contrast of shadow texture created by the air–water interfaces of the flow. The shadow texture then serves as tracers for velocity determination by cross-correlating consecutive images. BIV has been successfully employed for velocity measurements of highly aerated flows in many studies, such as green water flow on offshore structures due to breaking wave impingement (Ryu et al. 2005, 2007a, b; Chang et al. 2011; Song et al. 2015; Chuang et al. 2015, 2017, 2018; Vidic-Perunovic et al. 2017; Raby et al. 2019), wave breaking in

deep water and on a sloping beach (Pedrozo-Acuña et al. 2011; Lim et al. 2015; Na et al. 2016, 2018), open channel flows and hydraulic jumps (Lin et al. 2008, 2012), and liquid sloshing (Song et al. 2013).

Based on the previous studies using BIV on aerated flows and wave–structure interactions, it is anticipated that using BIV may be a useful approach for the study of a tsunami bore interacting with a simplified structure at different headings. On the other hand, using the optical flow method may be another promising approach to study such flows. Several studies have employed this technique to quantify aerated flows in stepped spillway (e.g., Bung and Valero 2016; Kramer and Chanson 2019). However, its applicability to violent flows in wave–structure interactions remains to be quantified.

The present study presents an experimental investigation of flow kinematics and hydrodynamic pressures and forces on a simplified coastal building under tsunami bore impact. A rectangular model structure sitting on a 1/10 sloping beach at four different headings, including 0°, 15°, 30°, and 45°, was used as the building. The scenario of a large long wave breaking on a relatively steep beach was created to mimic a tsunami bore of the high run-up intrusion type. The high-speed bore then traveled inland on the sloping beach and eventually impacted on structures of different heading with respect to the bore propagation. In the study, the flow velocities in aerated bore region were measured using the BIV technique. Pressure measurements were also taken at four points along a vertical line to obtain the impact pressure distribution on the frontal wall of the model structure. In addition, a multi-axis load cell was used to measure impact forces in the surge direction. To evaluate the turbulent flow field, simultaneous and synchronized measurements of velocity, pressure, and force with identical initial and boundary conditions were repeated 20 times for each structure heading so mean quantities of the physical variables can be determined. In the paper, the flow patterns, velocity fields, and maximum velocities will be demonstrated. The validity of the dam break model for a sloping bed will be examined. Features of the impact pressures and the relation between impact pressures and flow velocities will also be examined. Finally, surge force modeling using the measured impact pressures will be shown, and comparisons between the modeled and measured peak surge forces will be presented and discussed.

2 Experiment setup

2.1 Facility and model structure

The experiment was conducted in the Directional Wave Basin, a three-dimensional wave basin, housed in the O.H. Hinsdale Wave Research Laboratory (HWRL) at Oregon State University. The dimensions of the basin are 48.8 m long, 26.5 m wide, and 2.1 m deep. A multidirectional, piston-type wavemaker, capable of generating maximum wave height of 0.8 m with a maximum stroke of 2.1 m, is positioned at one end of the basin. The other end is a 1/10 sloping beach (slope $\theta_s = 5.7^\circ$) with its toe locating at 24 m from the neutral position of the wavemaker paddles.

The wave basin was filled with freshwater with a constant still water depth $h = 0.50$ m at the flat-bottom section throughout the experiment. The experiment setup and the locations of three capacitance-type wave gauges (termed WG1 to WG3) are sketched in Fig. 1. The simplified model structure was constructed using marine plywood and positioned on the sloping beach at a horizontal distance 8.35 m from the toe of the sloping beach

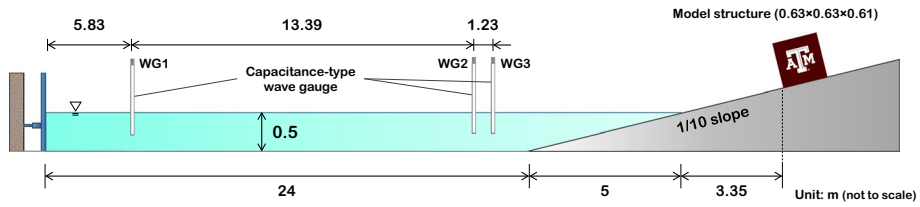


Fig. 1 Schematic diagram of the experiment setup in the wave basin from elevation view. Note that the wavemaker is at the left end and the waves propagate from left to right

or 3.35 m from the stationary water line. The model structure has dimensions (LWH) of $0.63 \times 0.63 \times 0.61 \text{ m}^3$. Two coordinate systems are used in describing the geometry and the physical properties in the study—one is defined as “basin-fixed coordinates” (x_B, y_B, z_B) with the z_B axis normal to the basin floor and the other defined as “slope-fixed coordinates” (x, y, z) with the z axis normal to the sloping beach. Figure 2a illustrates both coordinate systems and origins—both defined at the bottom of the centerline on the front wall of the model structure. In addition, Fig. 2b sketches the model structure from plane view at the four different headings, including $\theta_b = 0^\circ, 15^\circ, 30^\circ,$ and 45° . The slope-fixed coordinate system is referenced in the data processing and analysis. However, in accordance with image coordinates, any physical quantities superimposed with the background images are presented in basin-fixed coordinates.

2.2 Wave condition

Traditionally, a tsunami wave is typically simulated by a solitary wave which (in theory) has an infinite wavelength. However, generating a solitary wave in a basin with a relatively short distance between the wave paddle and the beach is not practical, while the wave amplitude would be also quite limited. To utilize the maximum stroke of that particular wavemaker, the alternative is to simulate a tsunami-like wave at landfall by programming the wave paddle motion to move as a single position surge over the full stroke length over 6 s, with the input signal designed as a 6-second error function. Figure 3a shows the mean free surface elevations averaged over 80 repeats measured by

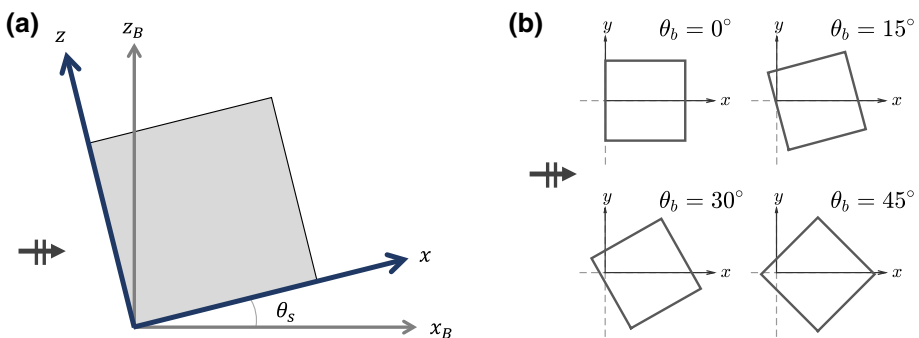


Fig. 2 **a** Definition of the basin-fixed coordinate system (on $x_B - z_B$ plane) and the slope-fixed coordinate system (on $x-z$ plane). **b** The four different structure headings in the slope-fixed coordinate system

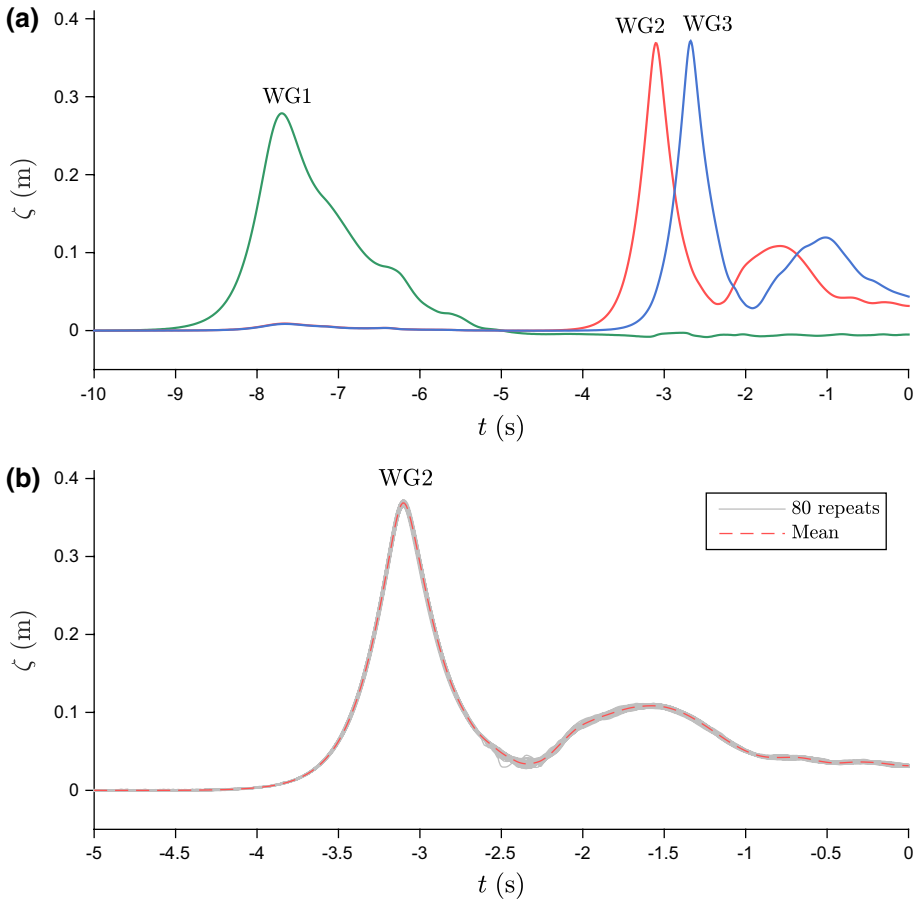


Fig. 3 **a** Mean free surface elevations measured by the three wave gauges. **b** Mean and instantaneous free surface elevations measured at WG2

the three wave gauges. Figure 3b compares the mean and 80 repeated free surface elevations at WG2. The comparison demonstrates a highly repeatable wave with a standard deviation of 5 mm (or 1.4% of the wave amplitude). At WG2 and WG3, it can be seen that the surge wave split into two successive waves in which the larger one is the target wave. Note that the smaller wave following the larger target wave did not influence the tsunami impact quantification so the impact can be considered as modeling a single tsunami wave impact. Using the surface elevation measured at WG2 as the input wave condition, the wave amplitude (A) is 0.37 m. After passing WG2 and traveling another 4.78 m, the waves shoaled on the beach, formed a plunging breaker, and finally impinged on the beach at a point roughly at the still water line. This wave condition created a high run-up intrusion type tsunami with a subsequent bore traveling at a high speed on the relatively steep beach.

2.3 Fluid velocity measurements

As the tsunami wave broke while shoaling, the flow kept traveling inland in the form of a bore. The wave breaking process and subsequent wave impact on a structure not only make the flow highly turbulent, but aerated by entraining air. To quantify such a turbulent aerated flow, the bubble image velocimetry (BIV) technique, introduced by Ryu et al. (2005), was employed in the present study. The concept of the BIV technique is to employ grayscale contrast in the images created by air–water interfaces within the depth of field (DOF) as tracer for cross-correlation. As a result, the flow velocities in the aerated region can be determined. It should be pointed out that the technique is based on tracking bubble motion so the measured velocities are the bubble velocities which may not be identical to the water velocity in aerated flows, especially when the bubbles are large. On the other hand, the technique would work well if the inertial force is much greater than the buoyant force.

To enhance the contrast in BIV images, a typical setup employs a backlit LED or a light diffuser illuminated by light bulbs (to mimic a LED) that provides a uniformly illuminated background. In the present experiment, a high-speed camera (Vision Research M340) was used. The camera has a maximum resolution of 2560×1600 pixels, a 12-bit dynamic range, and a maximum framing rate of 800 frames per second (fps) at full resolution. Since the camera is of high light sensitivity, preliminary tests indicated that no additional backlit illumination sources are needed to enhance the contrast. The high-speed camera was installed at a height of 5.29 m from the bottom of the model structure, as shown in Fig. 4a.

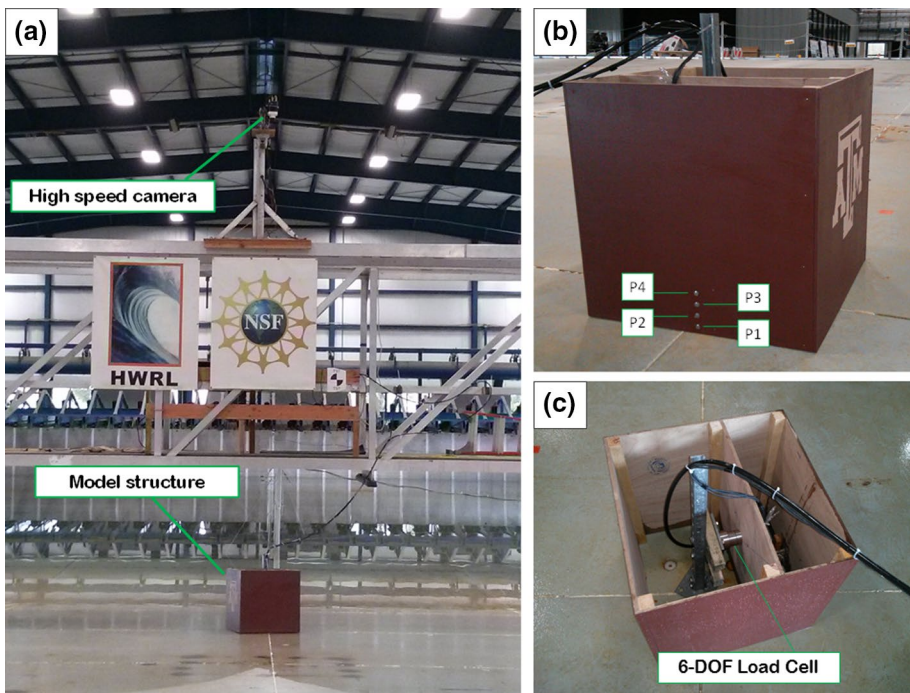


Fig. 4 Pictures of instrumentation. **a** The relative position between model structure and high-speed camera. **b** The vertical array of four pressure sensors at $y=0$. **c** The six-degree-of-freedom load cell

It was pointed downward, covering a field of view (FOV) of $2.66 \times 1.66 \text{ m}^2$. The framing rate was set at 500 fps throughout the experiment. A Nikkor 50-mm $f/1.4$ focal lens was mounted on the camera, and the horizontal focal plane was set at 0.1 m above the slope at the leading edge of the model at $\theta_b = 0^\circ$ heading. Note that the focal plane is parallel to the $x_B - y_B$ plane. The DOF was set to 0.53 m with the f -number equal to 1.4, enabling a sufficient vertical coverage with the geometric error on measured velocity magnitude within 5%. Note that the error reduces by $1/\sqrt{N}$, with N being the repetition number. Accordingly, the geometric error is merely 1% since there were 20 repeated tests for each structure heading. In the image processing using cross-correlation, the interrogation window was set to 32×32 pixels with a 50% overlap between two adjacent windows, resulting in $17 \times 17 \text{ mm}^2$ in spatial resolution in velocity measurements. More details on the principles, validation, applications, and discussion regarding to the BIV technique can be found in Ryu et al. (2005, 2007a), Chang et al. (2011), Lin et al. (2012), Song et al. (2013), and Chuang et al. (2015, 2018).

As the BIV technique is for two-dimensional velocity measurements (on the x - y plane in the present study) within the limited depth of view, it provides no information on the velocity variation in the third (z) direction. As a result, the measured velocities were assumed as the depth-averaged velocities since the DOF covers the entire water depth of the bore. The assumption would be likely true if the bubbles are evenly distributed over the depth. After examining the BIV images, we found that the bore front contains significant air entrainment over the entire water depth. The measured velocities in that region can be viewed as depth-averaged velocities. That region is indeed the most important region because of its high fluid velocity and its contribution to the peak impact magnitude. For the region behind the highly aerated bore front, the air bubbles were mostly generated from the wave breaking process. The number of bubbles is relatively low but sufficient for BIV velocity determination. Buoyancy may fuel these air bubbles to rise so the measured velocities are more likely to be surface velocities. Tracking the bubble positions in the z direction is not possible since the measurements were only available on the horizontal plane. Nevertheless, based on the measured vertical profiles of surge velocities reported by Smith and Lisa (2014) and Wüthrich et al. (2016), the bubbles are most likely to float in the region above the viscous sublayer, while such region has a nearly uniform velocity distribution along the z axis. As a result, each surge velocity determined by tracking the bubbles may be assumed uniform in z .

2.4 Pressure measurements

Pressure measurements were taken at four evenly spaced points on the frontal wall of the model structure, termed P1 ($z = 20 \text{ mm}$), P2 ($z = 50 \text{ mm}$), P3 ($z = 80 \text{ mm}$), and P4 ($z = 110 \text{ mm}$), as shown in Fig. 4b. Four piezoresistive pressure sensors (Kistler 4053A1) were mounted with great care to ensure that the wall surface remained flush. The sensors measure pressure differential referenced to the surrounding atmospheric pressure with a range up to 1 bar and a sensitivity of 200 Pa/mV. The natural frequency of the sensors is higher than 15 kHz. In the present experiment, the pressure measurements were sampled at 10 kHz.

2.5 Force measurements

A six-degree-of-freedom load cell (UDW3-500) was used to measure forces and moments acting on the model structure. In HWRL, the basin slope is made of steel plate with pre-drilled holes for instrument/model mounts, and no intrusive modification (such as drilling a sizable hole to accommodate the load cell and its cable) was allowed. As a compromise, one side of the load cell was bolted on a steel plate that was firmly fixed on a sturdy steel bar. The steel bar rigidly stood at an angle normal to the sloping beach with its base plate bolted on the beach. The other end of the load cell was directly attached to the inner vertical wall of the model structure by bolts. Note that the longitudinal centerline of the load cell passed through the center of gravity of the model structure. The above description is reflected in Fig. 4c. Heading of the model structure was changed by rotating the base of the steel bar along with the model structure and the load cell. It should be noted that only the surge forces (in the positive x direction) are of interest in the present study. The force and moment measurements were sampled at 500 Hz, while the natural frequency of this force transducer is higher than 700 Hz.

2.6 Measurement procedure

Measurements of pressures, fluid velocities, free surface elevations, and surge forces were simultaneously performed. The synchronization over different instruments was achieved by employing a rising-edge trigger signal sent 20 s before the wavemaker initiation. Note that the uncertainty of the analog trigger from the HWRL DAQ system is ± 7 ms. For high-speed imaging, an additional delay was programmed through the camera control panel to ensure that each event was captured during the 4-s short recording window. In the experiment, each structure heading was repeated 20 times with identical initial and boundary conditions so a total of 80 identical waves were sent. Before further analysis, the measured physical quantities were transformed to the slope-fixed coordinate system for consistency. The corresponding mean quantities were obtained by ensemble averaging the 20 repeated instantaneous data in each heading. Note that $t=0$ is defined as the moment when the bore reached the leading edge of the model structure at the $\theta_b=0^\circ$ heading.

3 Results and discussion

3.1 Flow patterns and maximum velocities

Figure 5 presents the flow evolution superimposed with the ensemble-averaged mean velocities measured by BIV for each structure heading. Note that the background images in the figure were randomly selected from one of the 20 repeated tests in each heading. Figures 6 and 7 further show the corresponding mean x -direction (U) and y -direction (V) velocity contour maps, respectively. The streamlines of the velocities were also plotted on top of the contour maps.

In Fig. 5, the flow is positive x -direction dominated before the wave impingement on the structure ($t < 0$) and the velocity profiles along the y axis seems uniform. Nevertheless, the shape of the bore front is irregular. Video recordings based on the 80 repeated tests show high irregularity of the bore fronts in both time and space. Yeh (1991) argued

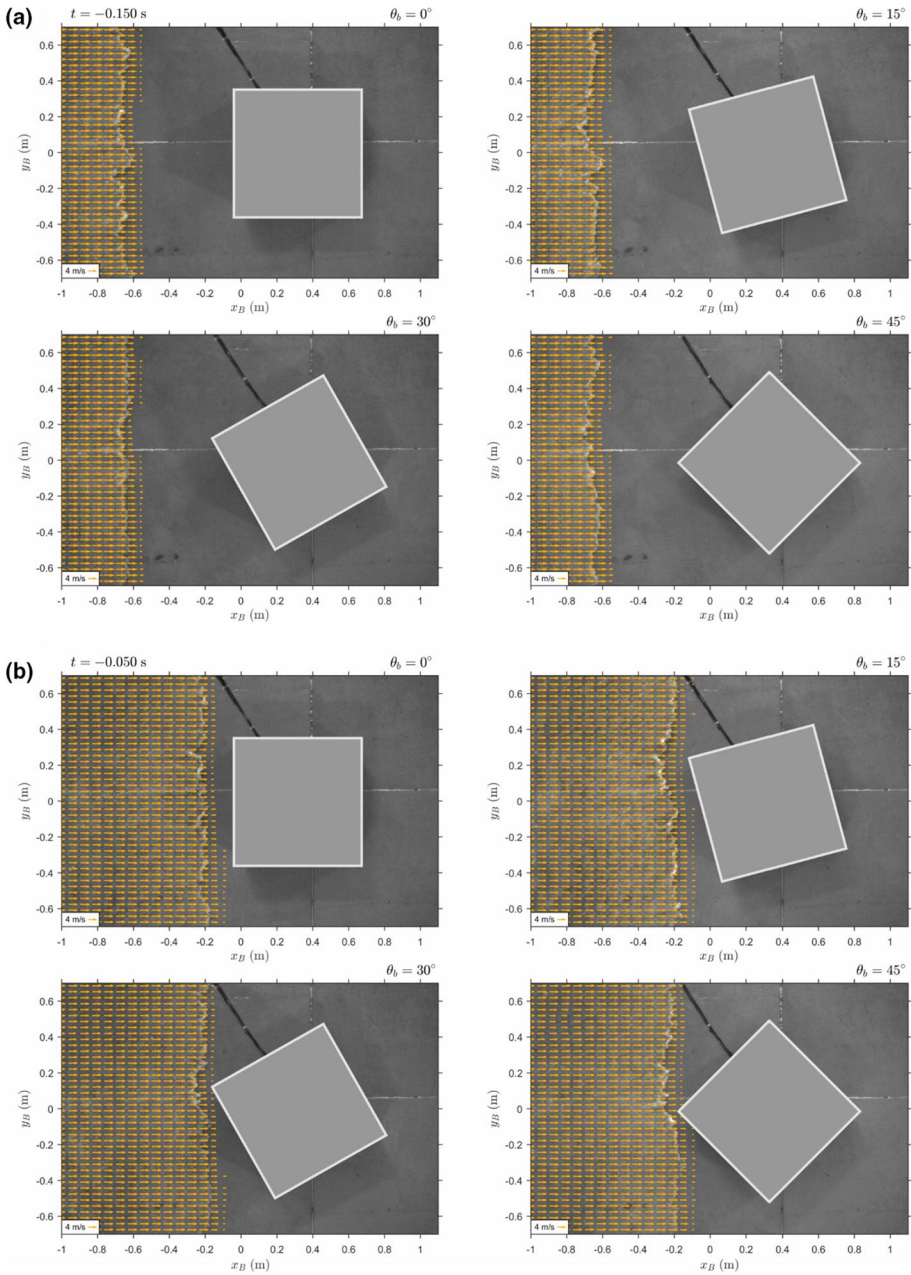


Fig. 5 Flow patterns and mean velocity maps for the four headings at $t = \mathbf{a} -0.150$ s, $\mathbf{b} -0.050$ s, $\mathbf{c} 0.070$ s, $\mathbf{d} 0.150$ s, $\mathbf{e} 0.200$ s, $\mathbf{f} 0.330$ s

that the irregularity and three-dimensional effects are mainly caused by the turbulent nature of the flow. The rough bore front can entrain air upon impact; the entrapped air may cause a gain in peak pressure (Bagnold 1939) and create pressure oscillation after

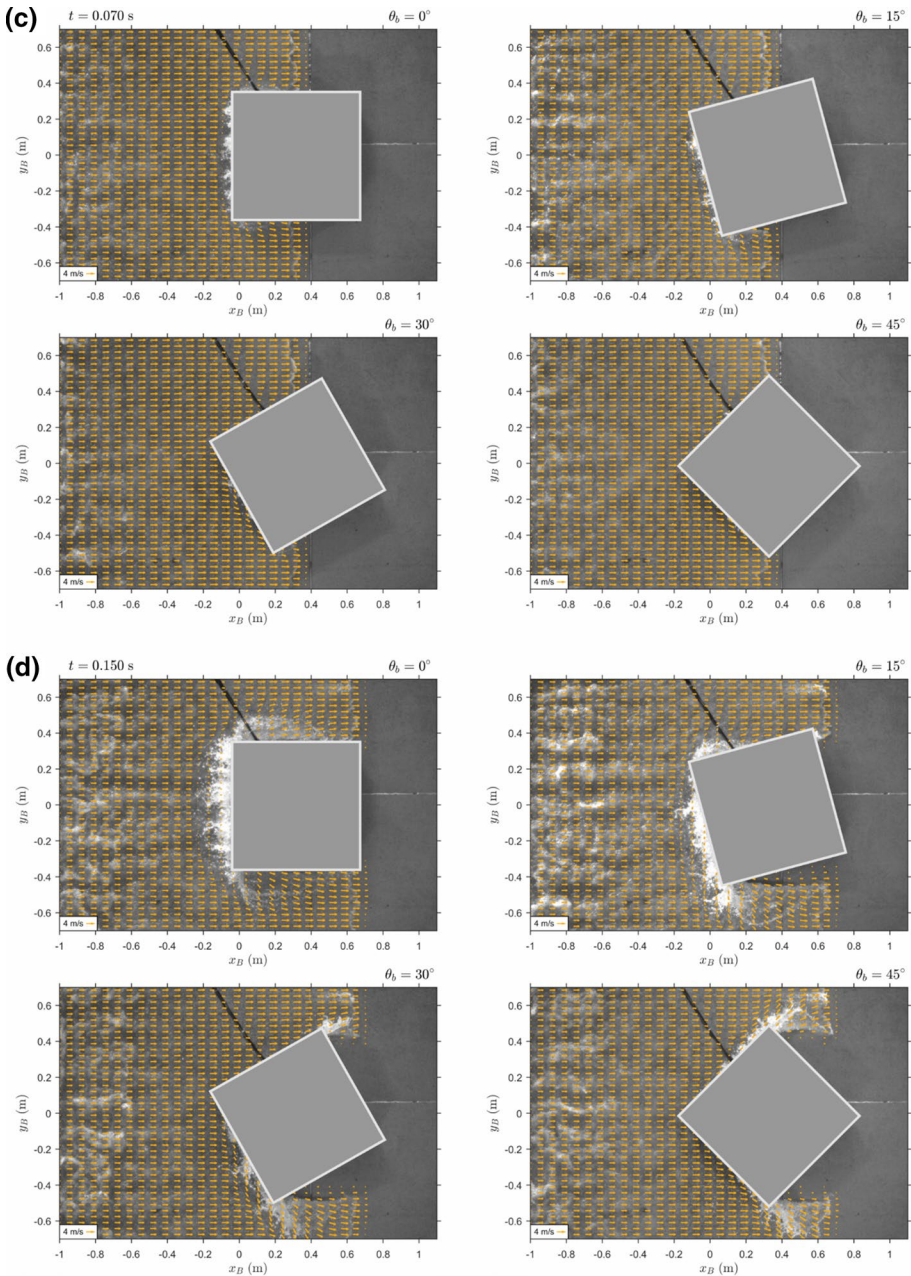


Fig. 5 (continued)

the peak pressure passes (Peregrine 2003). Furthermore, the transition from wave to bore (through a plunging breaker impinged on a sloping beach in this study) results in significant air entrainment. The entrained air could make the pressure time history even more complex due to the mechanism of damping the impact pressure by air cushioning

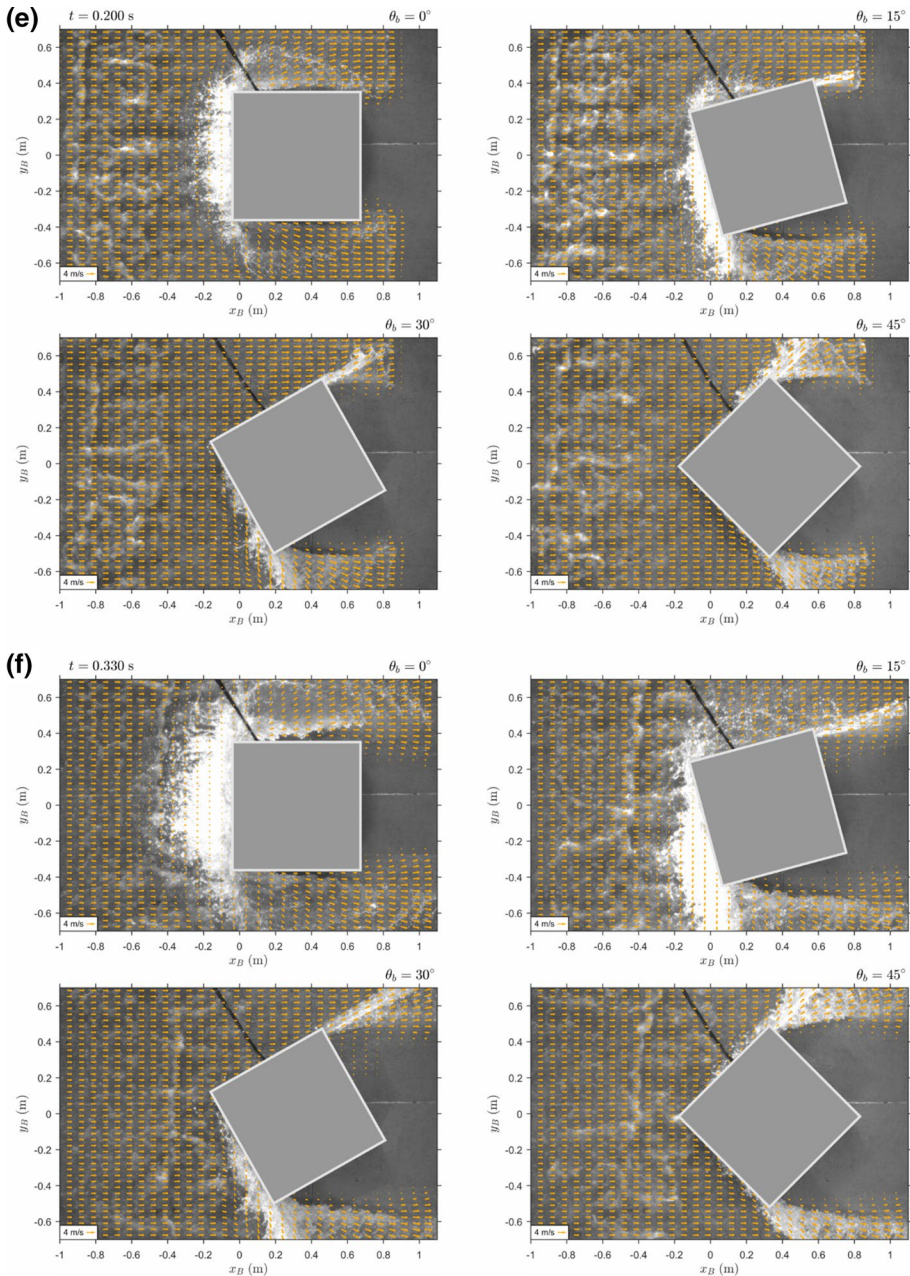


Fig. 5 (continued)

effect and amplifying the impact pressure due to compressed air (Peregrine 2003; Chuang et al. 2018).

By examining the flow deflection and reverse patterns in Figs. 5, 6 and 7, the $\theta_b = 0^\circ$ heading seems to be the worst-case scenario in terms of impact force based on the rate

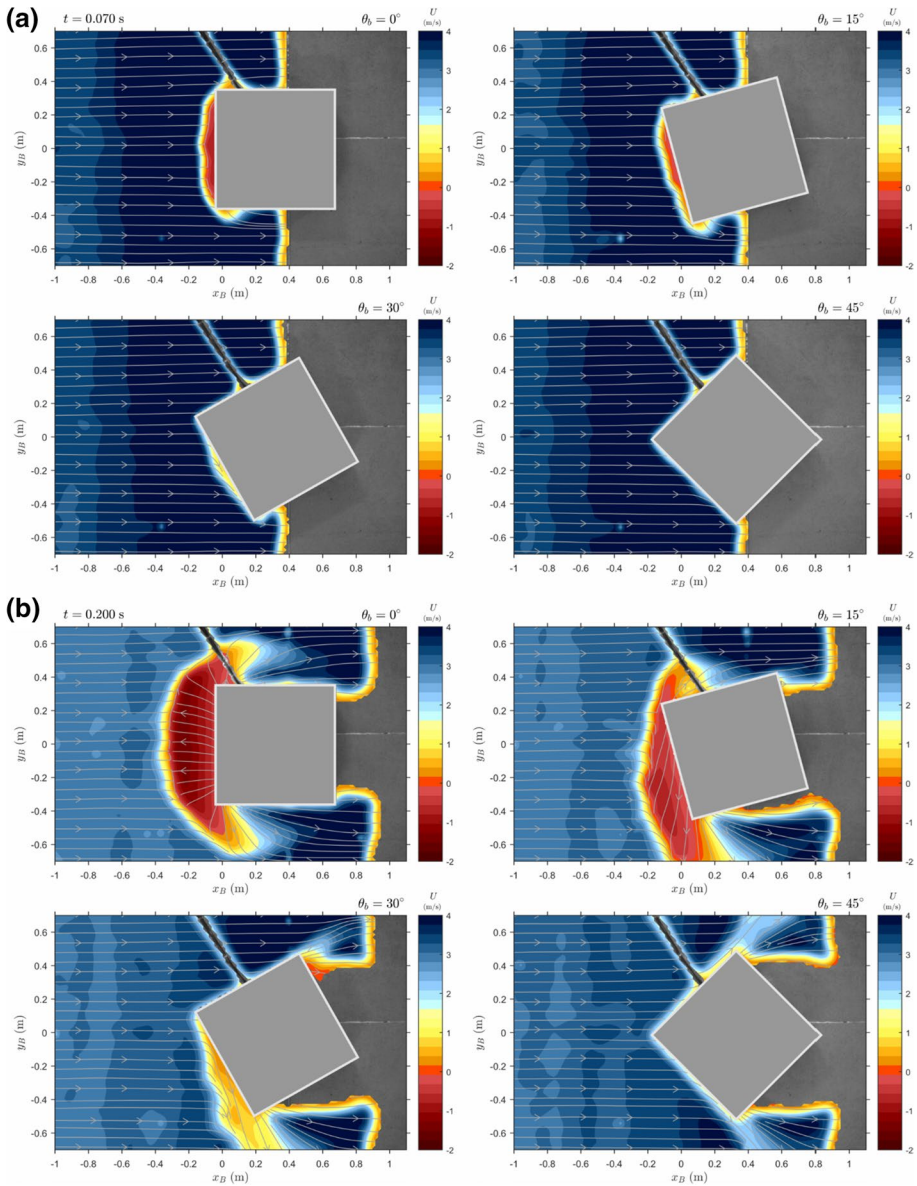


Fig. 6 The U velocity contour maps with streamlines for the four headings at **a** $t = 0.07$ s (corresponding to Fig. 5c) and **b** $t = 0.20$ s (corresponding to Fig. 5e). The black line in each figure is the umbilical cable for the sensors

of change of linear momentum. Similarly, the deflection and reverse patterns reduce, indicating a possible reduction of impact severity, as the angle of heading increases. Although the images and flow measurements are two-dimensional, the large area of negative U velocities implies the occurrence of a violent reverse flow. One can see that the reverse flow at the $\theta_b = 0^\circ$ heading is the strongest, i.e., with the highest U velocity

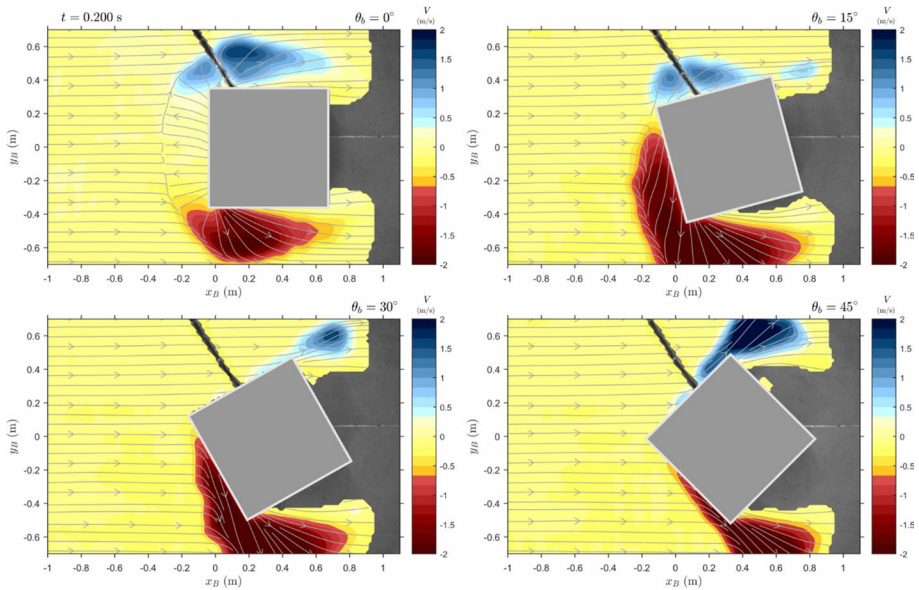


Fig. 7 The V velocity contour maps with streamlines for the four headings at $t=0.20$ s, corresponding to Figs. 5e and 6b

magnitude and largest area coverage in the negative x direction, as shown in Fig. 6b. With increasing heading angle, the area of reverse flow shrinks, and more incoming flow was deflected by the structure sidewalls instead of bouncing back from the structure wall and becoming a reverse flow. On the contrary, the low or zero velocity “wake” area behind the structure also expands with the increase of the heading angle and so as the projecting area. It may be straightforward to predict that the impact pressures on the structure wall are the highest in the zero heading case. Nevertheless, it is far from trivial to predict whether the total surging forces decrease (or increase) with increasing heading angle.

Figure 8 presents the time histories of the local maximum U velocity over the entire ensemble-averaged flow field in both positive and negative x directions ($|U_+|_{\max}$ and $|U_-|_{\max}$) and the local maximum V velocity in both positive and negative y directions ($|V_+|_{\max}$ and $|V_-|_{\max}$) for the four headings. In Fig. 8a, $|U_+|_{\max}$ decreased continuously and linearly with time as the bore propagated on the sloping beach before impinging on the structure. Upon the impact at $t = 0$, the magnitude of the or so-called the impact velocity (U_{imp}) reached 4.61 m/s or $U_{\text{imp}} = 1.58\sqrt{g(h+A)}$ (or 1.58 times of tsunami wave speed) with g being the gravitational acceleration normal to the basin floor. Note that the magnitude of U_{imp} is the same among the four headings, so it is subsequently used as the velocity scale for normalization. After the impact, $|U_+|_{\max}$ is expected to stay near the bore front (in region undisturbed by structure). However, the FOV was not wide enough to cover the undisturbed bore front, so the data points in Fig. 8a are intentionally plotted in light gray. During post-impact, the magnitude of $|U_-|_{\max}$, which is associated with the reverse flow, becomes smaller as the heading angle gains. For the maximum magnitude in transverse velocities, Fig. 8b shows an expected symmetric distribution in space between $|V_+|_{\max}$ and $|V_-|_{\max}$ at $\theta_b=0$ and $\theta_b=45^\circ$ with the largest value (up to 2.79 m/s or $0.61U_{\text{imp}}$) measured at the $\theta_b=45^\circ$ heading.

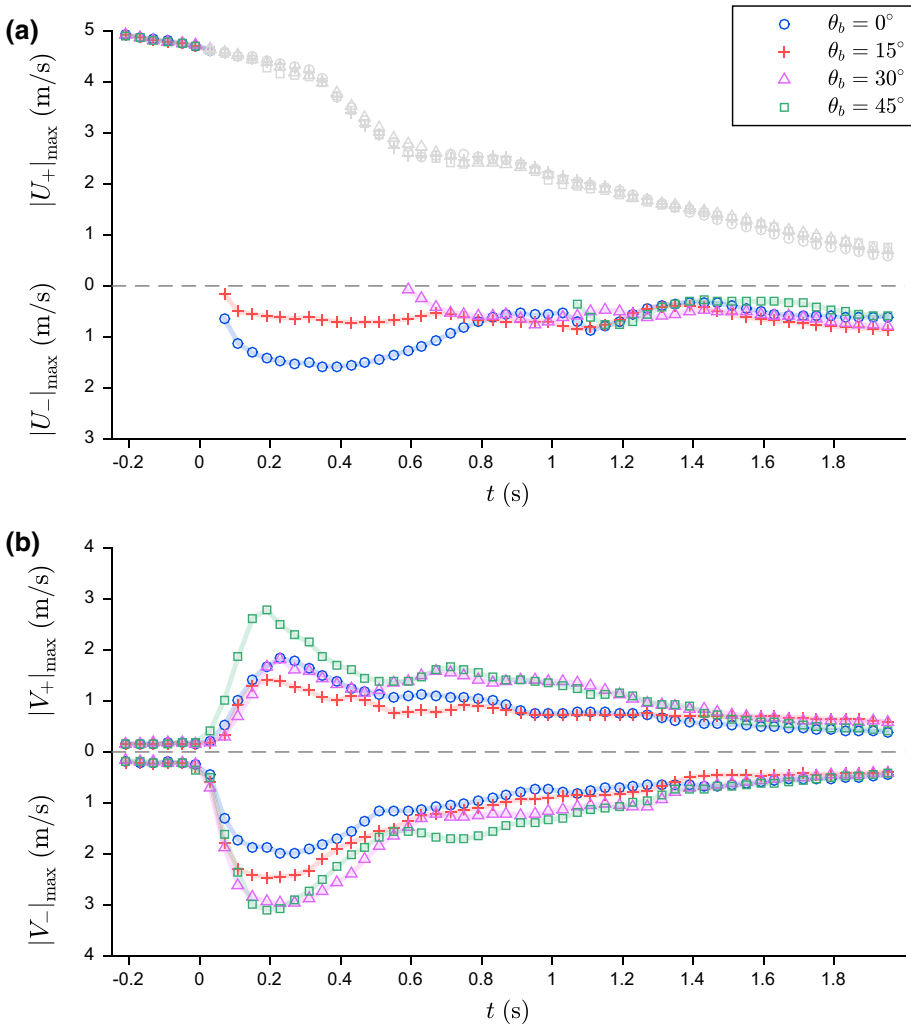


Fig. 8 Time history of **a** the maximum U velocity magnitude in both positive and negative x directions and **b** the maximum V velocity magnitude in both positive and negative y directions from the entire velocity field for the four headings. Note that the maximum U velocity magnitude in the positive x direction after $t=0$ (in light gray) is plotted after the front passed the FOV. The subscripts “+” and “-” indicate the positive and negative directions, respectively

3.2 Validity of dam break modeling of tsunami bore

Several studies (e.g., Chanson 2006; Kihara et al. 2015; Shafei et al. 2016) have shown that the kinematics of bores caused by tsunamis may be mathematically described by analytical dam break flow solutions to the Saint–Venant equations. The validity of dam break modeling is less an issue for most previous experimental studies since an actual dam break flow (or similar) was employed to simulate the tsunami bore impact. In the present study, a tsunami bore was generated by a large propagating wave breaking on a relatively steep slope. A typical

dam break flow bears no resemblance to the transient process from a propagating wave to a bore. Nevertheless, green water flows and bores are very similar; some studies (Ryu et al. 2007a, b; Chuang et al. 2015, 2018) have shown that a dam break flow can describe the green water velocity distribution in the fully developed stage well. Accordingly, the present study examined the validity of modeling the bore velocity distribution in a one-dimension sense as a dam break flow. In addition, an empirical coefficient obtained from the measurements was used to evaluate the conversion of initial water depth in the dam break flow from the wave characteristics.

For a frictionless channel with a constant mild slope $S_o = -\sin \theta_s$, Chanson (2006) derived an analytical dam break solution to the Saint–Venant equations. The celerity (U_c) and velocity (U) profile of the flow can be expressed as:

$$U_c = 2\sqrt{gh_D} + S_o g t_D \quad (1)$$

$$U = \frac{2}{3} \left(\sqrt{gh_D} + \frac{x_D}{t_D} + S_o g t_D \right) \quad (2)$$

where h_D is the initial water depth of the reservoir, t_D is elapsed time with $t_D = 0$ being the instant of dam removal. The solution is valid over $-\sqrt{gh_D} \leq x_D/t_D \leq 2\sqrt{gh_D} + \frac{1}{2}S_o g t_D$ in which x_D is the downstream direction with $x_D = 0$ being at the dam. For $S_o = 0$, both Eq. (1) and Eq. (2) reduce to the classical solution of Ritter (1892). Unlike a sudden release of a large water mass at the dam in the dam break flow, the transformation from tsunami wave breaking to bore propagation on beach makes it difficult to define $x_D = 0$ explicitly. To simplify the complexity, the present study matches the dam location to the breaking wave impingement point at $x = -3.37$ m or $x_D = 3.37$ m. To determine the initial water depth, $h + A$ was assumed to be a suitable approximation. However, preliminary trials showed that the use of $h + A$ in this manner led to significant overestimation by 24%. This is expected since the loss of horizontal momentum in wave breaking processes was not taken into account. To incorporate this factor in a straightforward manner, a coefficient was added. With this concept, a new form of initial depth $h_D = \alpha(h + A)$ is proposed for Eq. (1) and Eq. (2), where α is to be determined by Eq. (1) using the measured bore celerity at $t = 0$. Figure 9 plots the x -direction bore front position against time before the bore impacting with the model structure at $x=0$ and $t=0$. The slope effect in such short distance (~ 1.2 m) is insignificant. A constant bore celerity $U_c = 4.29$ m/s or $1.47\sqrt{h + A}$ is observed near $t = 0$. By examining the video, $t_D = 0.633$ s was obtained at $t = 0$. With the above inputs available, Eq. (1) gives $\alpha = 0.60$.

On the other hand, on the basis of Eq. (1), Chanson (2009) derived another solution that further implements a reservoir initially at a speed of $\sqrt{gh_D}$. This gives a more realistic mathematical description on the transition from a wave to a bore on a sloping beach. The mathematical description has an implicit form which can be expressed as:

$$\frac{32}{13} \left(1 + \frac{1}{2}\sqrt{gh_D} + \frac{1}{2}S_o t - \frac{1}{2}U_c \right)^{7/2} = tU^2 \left(3.65 \times 10^{-5}k_s + \nu \frac{2.5 \times 10^{-3}}{\sqrt{gh_D^3 U_c}} \right)^{1/4} \quad (3)$$

where ν is kinematic viscosity of water and k_s is dimensionless equivalent roughness height. By assuming frictionless ($k_s = 0$) which is negligible for high-speed bore, $U_c = 4.13$ m/s

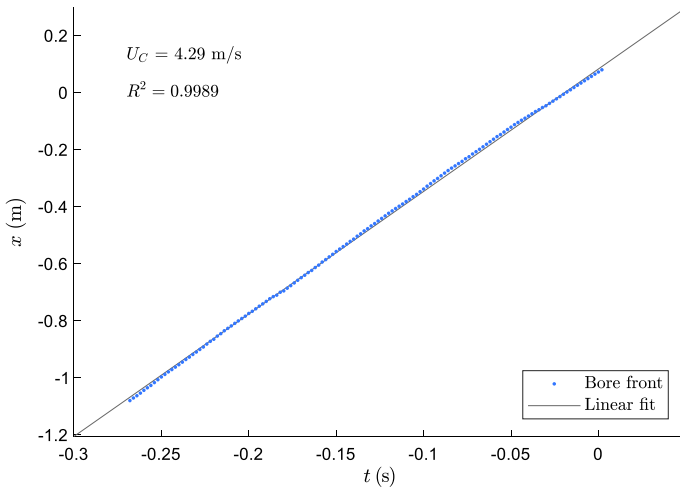


Fig. 9 Time history of bore front propagation before impact with the structure at $x=0$ and $t=0$

was calculated by numerically solving Eq. (3). The value is close to the measured bore celerity. In spite of the wave breaking process being ignored, Eq. (3) may be considered a reliable approach for approximating the bore celerity of high run-up intrusion type.

Figure 10 further shows the measured velocities against Eq. (2) with $S_o = -\sin \theta_s$ and $S_o = 0$ before the bore impacts the structure. Note that the U velocities distribution was determined by averaging the measured U velocities over the y direction. The figure clearly shows that Eq. (2) with a nonzero slope is able to capture the bore velocity distribution quite well. Although an actual bore velocity distribution is nonlinear, the comparison indicates that the use of Eq. (2) for engineering purposes may be simple and sufficient. Nonetheless, one should be aware that the solution is very sensitive to the initial water depth h_D and the value of α may be case specific. More work on examining the α value under various conditions is required to examine the validity of this approach.

3.3 Tsunami bore impact pressures

Figure 11 presents the time histories of the ensemble-averaged pressures taken at the four elevations of the pressure sensors, P1 to P4 located at $z=20$ mm, 50 mm, 80 mm, and 110 mm, respectively, for each of the four headings. In the figure, impulsive pressures, which reach a high pressure peak within a short rise time (Nouri et al. 2010; Kihara et al. 2015), can be observed at elevations P1 to P3. Note that rise time of less than 50 ms is typically referred as short. The impact caused by the high-speed bore front obviously accounts for the impulsive pressures. The subsequent bumps in the pressure time series are associated with the passage of the flow and the accumulated water due to the obstruction. Table 1 further summarized the peak pressure (P_{max}) and pressure rise time (t_r) for each measurement point. Based on Table 1 and Fig. 11, a trend is consistently observed: The magnitude of P decreases with the increase in heading angle and measurement elevation. Furthermore, the trend of t_r is opposite of that of P_{max} in most of the cases except at P1 with 0-deg heading in which the highest pressure reached 11 kPa (or about 10 times the corresponding hydrostatic pressure).

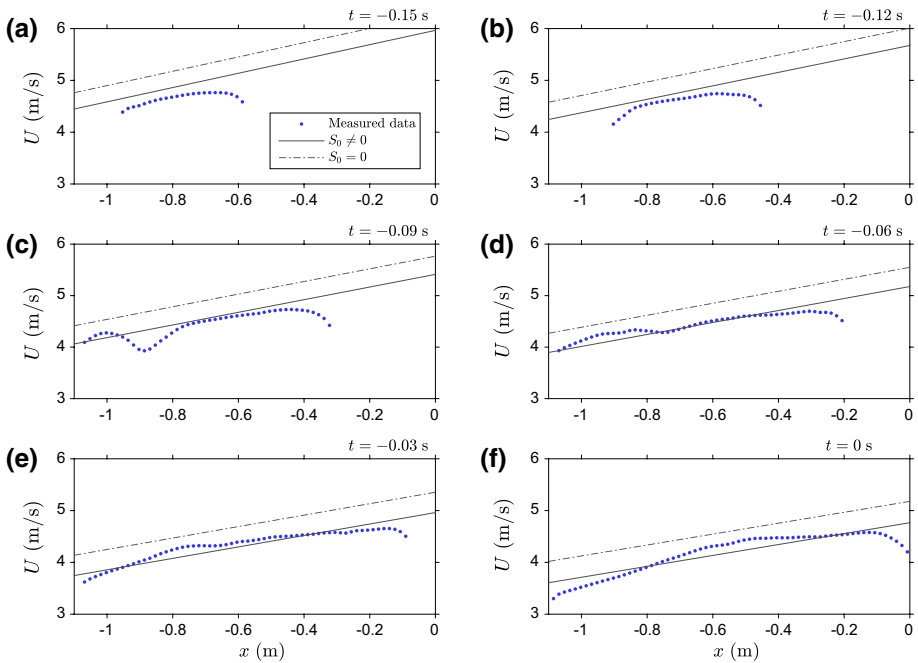


Fig. 10 Comparisons of the measured U velocity distributions and the analytical solutions for the bore flow before impact. *Solid line*, solution from Chanson (2006); *dotted-dashed line*, solution from Ritter (1892)

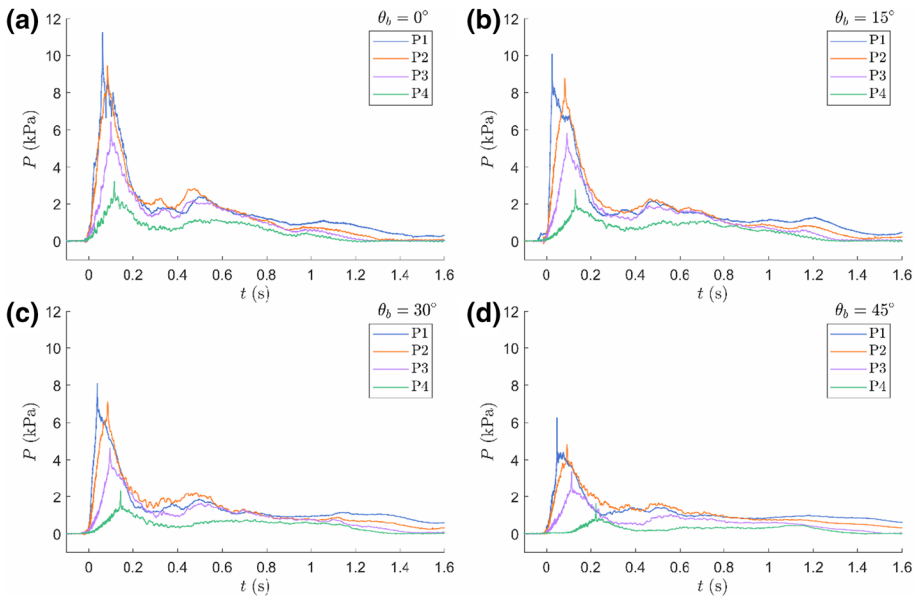


Fig. 11 Mean pressure time histories at four measurement points P1, P2, P3 and P4 located at $z=20$ mm, 50 mm, 80 mm, and 110 mm, respectively, for the four headings

Table 1 Summary of pressure measurements and impulsiveness

Measurement point	z (mm)	θ_b (deg)	P_{\max} (Pa)	t_r (ms)
P1	20	0	11,266	62
		15	10,067	27
		30	8094	38
		45	6262	49
P2	50	0	9455	83
		15	8782	85
		30	7110	84
		45	4845	94
P3	80	0	6449	99
		15	5834	94
		30	4657	94
		45	3373	114
P4	110	0	3235	113
		15	2808	132
		30	2342	141
		45	1625	223

In the present study, the bore height at the frontal wall was approximated as 0.041 m (the approximation method will be discussed in the next section), meaning that the measurement points at P2 (at $z=0.05$ m) and above mostly experienced “indirect impact.” Such impact was mainly caused by the presence of the model structure that redirected the incoming flow featuring strong x -direction momentum. Upon the impact, the obstruction of the model structure forced some water to pile up in front of the wall. Consequently, pressure measurement points above the bore height (P2–P4) began to sense impact and experience high pressure. During the process, some horizontal kinetic energy was transferred to potential energy, with some used to feed the W velocity momentum, which in turn forms run-up. As a result, the horizontal pressure magnitude reduced with higher elevation. The indirect impact reflects a symmetric or church-roof distribution (Peregrine 2003) as shown in Fig. 11.

Figure 12 shows the vertical distribution of peak pressures with linear regression for each heading. It is notable that the pressure distributions are nearly linear and resemble hydrostatic pressure, except with a magnitude much greater than that of hydrostatic pressure alone. For example, the zero heading pressure is about 10 times of hydrostatic pressure. Furthermore, another interesting aspect in the figure is that the projected zero-pressure heights or virtual surface for the four heading appear to be clustered near $z=0.146$ m. This observation is likely associated with the fact that an identical bore wave is impacting an identical vertical wall over all heading angles. However, detailed mechanism of determining the common virtual surface height is not clear and needs to be investigated in the future work with higher spatial resolution of pressure measurements.

The pressure distributions indeed deviate somewhat from straight lines, agreeing with what Robertson et al. (2013) observed in their study of a vertical wall impacted by a solitary wave at a much larger physical scale with more pressure measurement points. For such a bore flow, density variation due to air entrainment (Robertson et al. 2013) and the nonlinear velocity profile at the bore front (Yeh 1991) may influence the

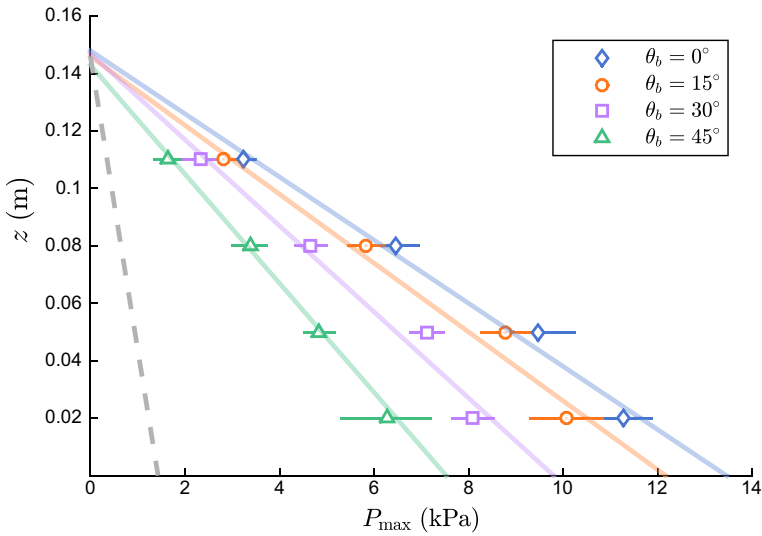


Fig. 12 Vertical distributions of peak pressures for the four headings. The *straight lines* are linear fits of the data for each heading. The average intercept point with a zero pressure is at $z=0.146$ m. Note that the *dashed line* represents the hydrostatic pressure distribution from $z=0.146$ m as a reference

magnitude of deviation. However, as suggested by Robertson et al. (2013), the hydrostatic-like assumption to the vertical profile of peak pressure may be valid for approximating resultant forces acting on a vertical wall. Accordingly, the assumption was applied to the subsequent analysis in the present study.

To facilitate their evaluation, impact pressures are frequently correlated with the local energy density. The ratio between an impact pressure and its corresponding local energy density is typically referred as the impact coefficient. The approach has been applied in many wave impact and green water impact studies (e.g., Chan and Melville 1988; Ariyaratne et al. 2012; Chuang et al. 2017). With the impact coefficient known, the peak pressure can be estimated by the measured or estimated velocity. That may overcome insufficient spatial resolution in pressure measurements, a typical problem in these experiments. In the present study, velocities were only measured on a horizontal plane while velocity distributions on the x - z plane were not available. That means correlating velocities with pressures at different elevations is not feasible. Alternatively, relating the maximum peak pressures (i.e., pressures measured at P1 under direct impact) with the measured maximum velocities was performed. Figure 13 shows peak pressures versus local kinetic energy density for the four headings. Note that the local kinetic energy density was evaluated in the direction normal to the pressure sensor end face. A linear least square fit forced to pass the origin was added to the figure as well. The impact coefficient is the slope of the linear fit. This slope is determined to be 0.55, with a coefficient of determination $R^2=0.95$. The straight line, nearly identical to the Bernoulli equation, seems to describe the relationship well. Density of water is used to represent the fluid density in the relation, but that is not strictly correct for a highly aerated flow. The absence of water density correction would contribute to the deviation, even though the relation seems to be quite linear. The accuracy of the correlation is likely to improve if the void fraction measurement is available (Ariyaratne et al. 2012; Chuang et al. 2017).

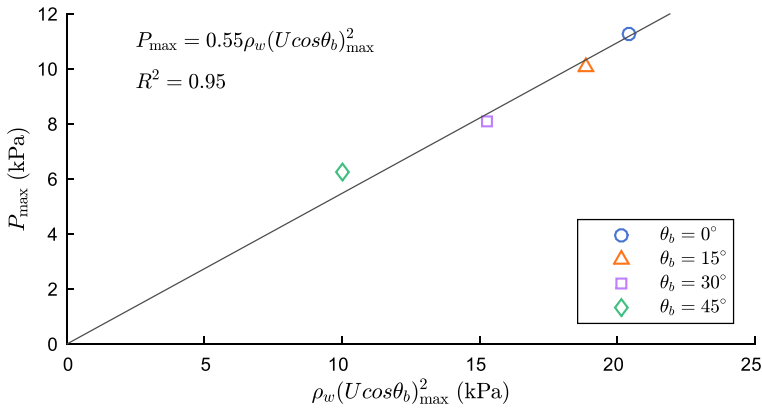


Fig. 13 Relation between the peak pressure and the local kinetic energy density

3.4 Estimating the tsunami bore height

Typically, bore height (h_B) measurements utilize wave gauges featuring electrical wires fixed by a solid stem. In the present study, a use of wave gauges would block the high speed imaging for BIV measurements. As a result, bore height measurements at the model structure were not directly performed in the present study. Nevertheless, the bore height is an essential input to the estimation of the surge forces (F_x) acting on the model structure. Despite having no direct measurement available, the bore height can be estimated from the relation between free surface height and flow velocity or the pressure–velocity relationship.

In this study, the estimation was made by employing the pressure–velocity relationship unveiled in Fig. 13 and the consideration of reverse flow. By assuming that the Bernoulli equation is valid for such transient flow, the peak pressure in the x direction may be simplified by summing up the hydrostatic pressure and the hydrodynamic pressure as:

$$P_{\max} = \rho_w g_n h_p + 0.5 \rho_w U_C^2 \tag{4}$$

where h_p is the ponding height (the sum of h_B and reverse flow height h_R), and g_n is the component of gravitational acceleration normal to the sloping beach. The h_R can be determined by adopting the formula derived by Robertson et al. (2011, 2013).

$$h_R = \left(\frac{U_C h_B}{\sqrt{g}} \right)^{2/3} \tag{5}$$

By using both Eqs. (4) and (5), h_B is calculated as 0.041 m, close to the visually observed estimate of about 0.05 m, so this value is used in the surge force modeling below.

3.5 Modeling the surge forces

The possibility of estimating surge forces (F_x) (i.e., the bore impact forces) by integrating measured pressures has been examined in some studies (Robertson et al. 2011, 2013; Shafiei et al. 2016). In practice, surge force modeling may vary with respect to problem of

interest and availability of measured data. The most straightforward setup of direct force measurement in most such experiments is to embed load cells beneath the model structure. However, as described in Sect. 2.5, a compromise had to be made in order to keep the steel bottom plate intact. As a result, the bottom static friction force is not negligible in the surge force modeling for a stationary model structure without additional fixtures between its bottom and the floor. Hence the modeled F_x is expressed as the sum of the maximum static friction force ($F_{s,max}$) and the integration of the measured pressures (F_{PS}), i.e.,

$$F_x = F_{s,max} + F_{PS} \tag{6}$$

in which the static friction force is calculated as:

$$F_{s,max} = \mu_{s,max} m_b g_n \tag{7}$$

where $\mu_{s,max}$ is the maximum static friction force coefficient, measured as 0.97 by applying a constant force (slightly larger than maximum static force) parallel to the sloping surface, and m_b (= 18 kg) is the mass of the model structure (including the pressure sensors). Note that the wave run-down force on the rear walls is assumed zero due to the fact that the flow momentum dominates in positive surge direction (+x).

The Thiessen polygons method was applied to calculate F_{PS} . Four evenly spaced intervals centered at each pressure measurement point were assigned. Uniform pressure distribution in each interval is assumed. To account for the reverse flow, an approximation was made by extending the upper boundary of the interval centered at P4 to the ponding height h_p . It is straightforward to apply the approximation to the $\theta_b=0^\circ$ heading case as it was also demonstrated by Robertson et al. (2011, 2013) and Shafiei et al. (2016). For the two asymmetric headings $\theta_b=15^\circ$ and $\theta_b=30^\circ$, pressures were only measured on one of the two walls facing the incoming flow. As shown in Fig. 14, the peak pressure and the angle of heading are related; an inverse proportional relationship was thus assumed. With this assumption, the pressures on the vertical walls at $\theta_b=60^\circ$ and $\theta_b=75^\circ$ headings were

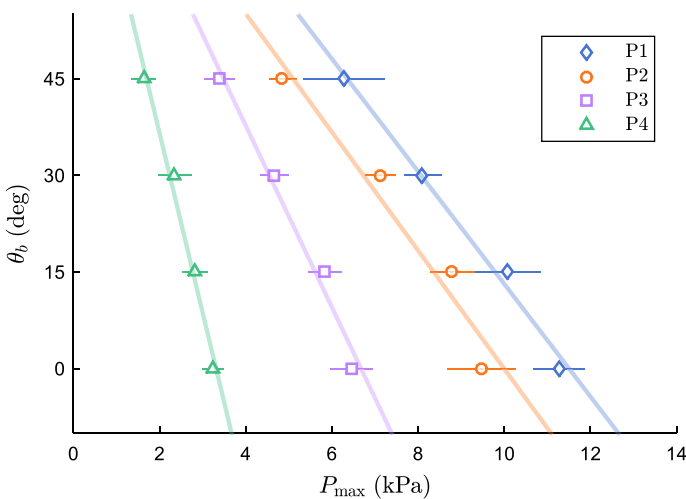


Fig. 14 Peak pressure versus angle of heading. The *straight lines* are linear fits of the data measured at the four elevations

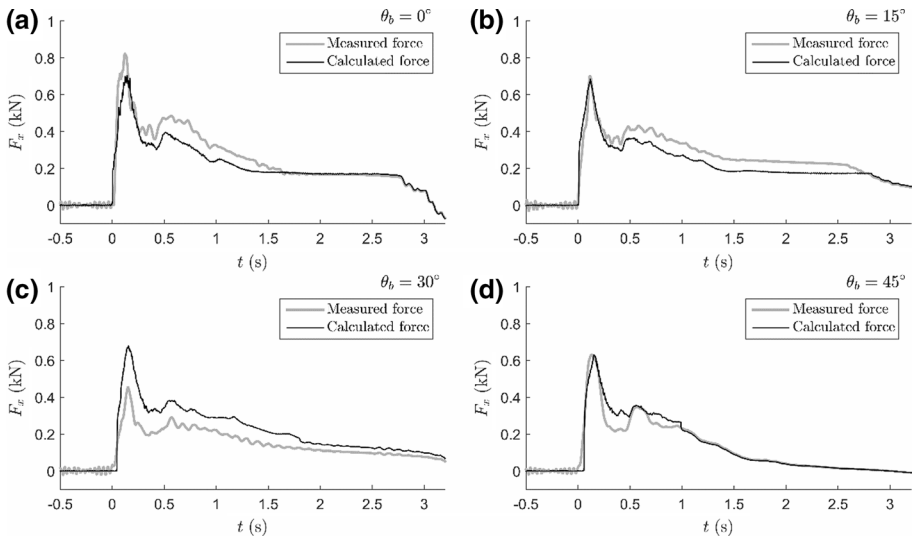


Fig. 15 Time histories of the calculated F_x and the measured F_x for the four headings

Table 2 Summary of calculated and observed reverse flow heights

θ_b	Calculated h_R (mm)		Observed h_R (mm)	
	Long side	Short side	Long side	Short side
0°	154	N/A	272	N/A
15°	150	62	209	84
30°	140	97	167	84
45°	122	122	167	167

interpolated. For the symmetric $\theta_b=45^\circ$ heading, F_{PS} was calculated by doubling the F_{PS} obtained from the wall with pressure measurements.

Comparisons of the time history between the measured F_x by load cell and the calculated F_x using Eq. (6) for the four headings are shown in Fig. 15. The comparisons indicate that the surge forces and pressure integrated forces are, while remarkably in phase, different in magnitude in most headings. For the $\theta_b=0^\circ$ heading, the calculated peak F_x values are roughly 117 N lower or 15% underestimated, whereas the calculated peak F_x value is around 227 N higher or 50% overestimated for the $\theta_b=30^\circ$ heading. The discrepancy may be explained by the following two main causes. Firstly, *accuracy in the h_R estimation*—Eq. (5) was derived based on the assumption of one-dimensional potential flow, and the horizontal variation of pressures is not being accounted for (more to follow). Table 2 lists the calculated and visually observed reverse flow heights. The overall discrepancy in the reverse flow height is similar to that in the peak forces in Fig. 15. Even if the calculated h_R is replaced by the observed value in the surge force modeling, it only improves the accuracy to an insignificant extent. Secondly, *horizontal variation of pressure distribution*—the present study took a vertical pressure profile at the center of a wall and assumed that the horizontal pressure distribution is uniform. This assumption may be unrealistic, especially for the $\theta_b=45^\circ$ heading in which a jet-like flow traveling along the wall was created due to

flow separation. With a relatively low speed, this separated flow traveling along the wall collided with the incoming bore and in turn affected the horizontal distribution of impact pressure on the wall. Even for the $\theta_b=0^\circ$ heading, the uniform pressure assumption may not apply to areas close to the corners.

Figure 16 compares the measured peak F_x (with error bars) and modeled peak F_x against the four headings, with the results extended to 90° because of symmetry. Note that F_x is normalized by the product of the water density, bore height, projected width (W_b), and squared impact velocity, implying the vertical axis has the form of a drag coefficient (C_D). Two approaches were used to model the peak F_x . The first approach (called *Modeled peak force I*) is that the peak surge forces are simply the peak values of the time series plotted in Fig. 15. The second approach or (called *Modeled peak force II*), following Robertson et al. (2013), estimates the peak forces using Eq. (6) but replacing F_{PS} by the integration of P_{max} with the assumption of hydrostatic-like vertical profile, i.e., integrating the area of each triangle in Fig. 12. Note that the vertical pressure distributions for the $\theta_b=60^\circ$ and $\theta_b=75^\circ$ headings (the sides without pressure measurements) were approximated by interpolating the assumed linear relationship from Figs. 12 and 14.

In Fig. 16, the relatively narrow error bars in the figure indicate that the variations of measured peak F_x values (ensemble averaged quantities) are moderate over experimental repetitions. The measured peak F_x values, as expected, have the maximum at the $\theta_b=0^\circ$ heading (with a magnitude of 842 N). Surprisingly, the minimum peak F_x value (=456 N) was measured at the $\theta_b=30^\circ$ heading, not at the $\theta_b=45^\circ$ heading. Treating the vertical axis in Fig. 16 as a drag coefficient C_D , we find that the distribution of C_D is different from the negatively correlated relationship between C_D and the angle of heading (from 0° to 45°) observed from the impact of a square prism by a dam break flow on a flat floor (Shafiei et al. 2016). The sudden drop in C_D at $\theta_b=30^\circ$ has not been reported, and the relatively high impact velocity in this study makes this physical behavior even more interesting. Examining the three-dimensional fluid–structure interaction may be the most possible way to reveal the cause. Unfortunately, the insufficiency in measurements hinders further investigation. On the other hand, the largest $C_D = 3.1$ was found at $\theta_b=0^\circ$. This value is about 50% higher than that reported by Arnason (2005) from a laboratory experiment

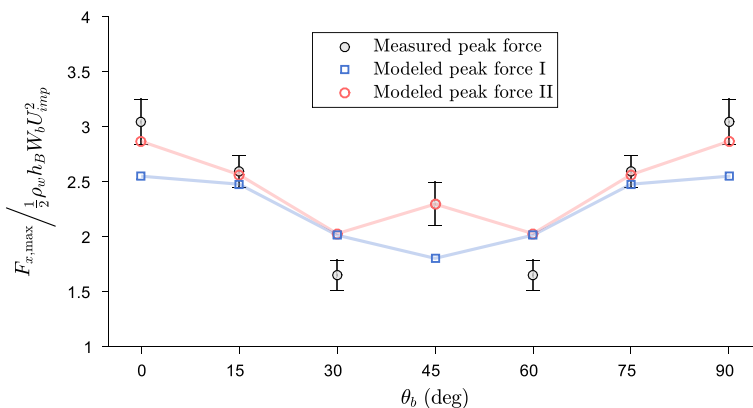


Fig. 16 Comparisons of normalized measured and modeled $F_{x,max}$ for the four headings. Note that “Modeled peak force I” was obtained from the peaks in Fig. 15, while “Modeled peak force II” was evaluated by integrating the peak pressures with respect to the heights in Fig. 12. The result was extended to 90° based on symmetry

using a square column at $\theta_b=0^\circ$ under a dam break bore impact. This is expected with much higher impact velocity caused by high run-up tsunami intrusion. Furthermore, the water density was generally used in evaluating C_D . In fact, the bore is highly aerated with entrained air bubbles, particularly at the bore front. If void fraction information is available, the C_D evaluated with corrected fluid density may increase (Ariyaratne et al. 2012; Chuang et al. 2017).

Comparing the modeled peak F_x by two approaches in Fig. 16, the *Modeled peak force II* captured the trend and magnitude much better than the *Modeled peak force I*. More importantly, the reduction of C_D at $\theta_b=30^\circ$ is only shown in *Modeled peak force II*. However, the questions concerning why *Modeled peak force II* yields a distribution similar to the measured one, and why *Modeled peak force I* fails to capture such a trend, remain to be answered. The finding may indicate that, for a prototype or some physical models in which force measurements are not feasible, the *Modeled peak force II* approach may be considered to approximate the peak surge force at various angles of heading.

4 Conclusions

An experimental investigation of tsunami bore impact on a simplified, square-shaped coastal building at four different headings ($\theta_b=0^\circ, 15^\circ, 30^\circ$, and 45°) was performed with measured fluid kinematic and hydrodynamic properties, including free surface elevations, impact pressures, impact forces, and two-dimensional horizontal flow fields. The high run-up intrusion type tsunami bore that creates high impact velocities was considered in designing the input wave condition. Instantaneous velocity fields of the aerated bore were measured using the BIV technique. For each heading, ensemble averages of forces, pressures, and flow velocities were obtained from 20 repeated tests with identical initial and boundary conditions.

By superimposing velocity contours with streamlines, the flow patterns clearly show how the tsunami bore interacted with the model structure at different headings. Before the impact, the flow is positive x -direction dominated. The maximum U velocity and the bore propagation speed were measured as 1.58 times and 1.47 times the tsunami wave speed, respectively. Hence, the tsunami wave was categorized as the high run-up intrusion type. During the impact, a significant influence by the angle of heading was found by examining the maximum V velocity. The maximum V velocity reached $0.61U_{\text{imp}}$ at the 45° heading. Violent reverse flows were observed in a form of splashing water at the $\theta_b=0^\circ$ heading.

For the velocity modeling, the dam break solution account for nonzero slope is found to be valid with properly approximated initial water depth. For the pressure measurements, the maximum mean pressure researched about 10 times the corresponding hydrostatic pressure at the $\theta_b=0^\circ$ heading. The measurement points from P2 to P4, located above the bore height, mainly sensed indirect impacts due to the pileup of the flow with strong x -direction momentum in front of the wall. The indirect impact pressures are of church-roof shape, comparing to the impulsive pressure characterized by a sudden increase in pressure followed up by a gradual decrease after reaching the peak. The vertical profiles of the peak pressure are close to a linear hydrostatic distribution. However, their magnitudes are one order higher than the corresponding hydrostatic pressure and inversely proportional to the angle of heading. By correlating the peak pressure with the corresponding local energy density, the impact coefficient was calculated as 0.55, close to the constant of 0.5 in the Bernoulli equation. With limited spatial resolution in pressure measurements,

the surge force modeling using measured pressure data agrees with the measured force to good degree. Based on the water density, bore height, projected width, and squared impact velocity, the maximum surge forces have a drag coefficient of 3.1. The peak surge force versus angle of heading was found to be better represented by directly integrating the pressure–elevation relationship—yielding good agreement in magnitude as well as capturing the variation with the lowest magnitude at the 30° heading.

Acknowledgements The authors wish to thank the financial support provided by Texas A&M Engineering Program and Pontificia Universidad Cantolica de Chile under the project entitled “Building Capacities to Withstand Extreme Coastal Wave Forces.” The authors would also like to thank Dr. Daniel Cox of Oregon State University for valuable discussion and inputs on the surge force modeling, John Goertz for valuable discussion in determining the input wave condition, and Dr. Pedro Lomonaco and his staff at Hinsdale Wave Research Center for assistance during the experiment.

References

- Ariyaratne K, Chang K-A, Mercier R (2012) Green water impact pressure on a three-dimensional model structure. *Exp Fluids* 53(6):1879–1894
- Arnason H (2005) Interactions between an incident bore and a free-standing coastal structure. PhD Dissertation, University of Washington, Seattle, WA, USA
- Asakura R et al (2000) An experimental study on wave force acting on on-shore structures due to overflowing tsunamis. *Proc Coast Eng* 47:911–915
- Bagnold RA (1939) Interim report on wave-pressure research. *Inst Civ Eng* 12:201–226
- Bryant E (2001) *Tsunami: the underrated hazard*. Cambridge University Press, Cambridge
- Bung D, Valero D (2016) Optical flow estimation in aerated flows. *J Hydraul Res* 54(5):575–580
- Cawley JG (2014) Review of guidelines for the design of tsunami vertical evacuation buildings. Master Thesis, Oregon State University, Corvallis, OR, USA
- Chan ES, Melville WK (1988) Deep-water plunging wave pressures on a vertical plane wall. *Proc R Soc London A Math Phys Sci* 417(1852):95
- Chang K-A, Ariyaratne K, Mercier R (2011) Three-dimensional green water velocity on a model structure. *Exp Fluids* 51(2):327–345
- Chanson H (2006) Analytical solutions of laminar and turbulent dam break wave. In: *International conference on fluvial hydraulics river flow*, Lisbon, Portugal, pp 465–474
- Chanson H (2009) Application of the method of characteristics to the dam break wave problem. *J Hydraul Res* 47(1):41–49
- Chinnarasri C, Thanasisathit N, Ruangrassamee A, Weesakul S, Lukkunaprasit P (2013) The impact of tsunami-induced bores on buildings. *P I Civil Eng Marit Eng* 166(1):14–24
- Chuang W-L, Chang K-A, Mercier R (2015) Green water velocity due to breaking wave impingement on a tension leg platform. *Exp Fluids* 56(7):1–21
- Chuang W-L, Chang K-A, Mercier R (2017) Impact pressure and void fraction due to plunging breaking wave impact on a 2D TLP structure. *Exp Fluids* 58(6):68
- Chuang W-L, Chang K-A, Mercier R (2018) Kinematics and dynamics of green water on a fixed platform in a large wave basin in focusing wave and random wave conditions. *Exp Fluids* 59:100
- Cross RH (1967) Tsunami surge forces. *J Waterw Harb Div ASCE* 93(4):201–231
- Fritz HM, Synolakis CE, McAdoo BG (2006) Maldives field survey after the December 2004 Indian Ocean Tsunami. *Earthq Spectra* 22(S3):137–154
- Fujima K, Achmad F, Shigihara Y, Mizutani N (2009) Estimation of tsunami force acting on rectangular structures. *J Disaster Res* 4(6):404–409
- Ghobarah A, Saatcioglu M, Nistor I (2006) The impact of the 26 December 2004 earthquake and tsunami on structures and infrastructure. *Eng Struct* 28(2):312–326
- Kihara N et al (2015) Large-scale experiments on tsunami-induced pressure on a vertical tide wall. *Coast Eng* 99:46–63
- Kirkoz M (1983) Breaking and run-up of long waves, tsunamis: Their science and engineering. In: *Proceedings of the 10th IUGG international tsunami symposium*
- Kramer M, Chanson H (2019) Optical flow estimations in aerated spillway flows: filtering and discussion on sampling parameters. *Exp Thermal Fluid Sci* 103:318–328

- Lim HJ, Chang K-A, Huang Z-C, Na B (2015) Experimental study on plunging breaking waves in deep water. *J Geophys Res Oceans* 120:2007–2049
- Lin C, Hsieh S-C, Kuo K-J, Chang K-A (2008) Periodic oscillation caused by a flow over a vertical drop pool. *J Hydraul Eng ASCE* 134(7):948–960
- Lin C, Hsieh S-C, Lin I-J, Chang K-A, Raikar RV (2012) Flow property and self-similarity in steady hydraulic jumps. *Exp Fluids* 53(5):1591–1616
- Linton D et al (2013) Evaluation of tsunami loads on wood-frame walls at full scale. *J Struct Eng* 139(8):1318–1325
- Liu H et al (2013) The 11 march 2011 Tohoku Tsunami survey in Rikuzentakata and comparison with historical events. *Pure Appl Geophys* 170(6):1033–1046
- Matsutomi H, Okamoto K (2010) Inundation flow velocity of tsunami on land. *Island Arc* 19(3):443–457
- Moon WC, Tan KC, Lau TL (2014) An experimental study on wave forces of tsunami on simplified onshore buildings at penang island, malaysia. *J Civ Eng Res* 4(3a):164–172
- Murty TS (1977) Seismic sea waves: tsunamis. Bulletin (Fisheries Research Board of Canada), No. 198. Department of Fisheries and the Environment Fisheries and Marine Service, Ottawa, Canada
- Na B, Chang K-A, Huang Z-C, Lim HJ (2016) Turbulent flow field and air entrainment in laboratory plunging breaking waves. *J Geophys Res Oceans* 121:2980–3009
- Na B, Chang K-A, Huang Z-C, Hsu W-Y, Chuang W-L, Chen YY (2018) Large-scale laboratory observation of fluid properties in plunging breaking waves. *Coast Eng* 138:66–79
- Nouri Y, Nistor I, Palermo D, Cornett A (2010) Experimental investigation of tsunami impact on free standing structures. *Coast Eng J* 52(1):43–70
- Palermo D, Nistor I, Al-Faelsly T, Cornett A (2012) Impact of tsunami forces on structures: The University of Ottawa experience. In: 5th International tsunami symposium
- Pedrozo-Acuña A, de Alegría-Arzaburu AR, Torres-Freyermuth A, Mendoza E, Silva R (2011) Laboratory investigation of pressure gradients induced by plunging breakers. *Coast Eng* 58(8):722–738
- Peregrine DH (2003) Water-wave impact on walls. *Annu Rev Fluid Mech* 35:23–43
- Raby A, Jayaratne R, Bredmose H, Bullock G (2019) Individual violent wave-overtopping events: behaviour and estimation. *J Hydraul Res* 58:34–46
- Rahman S, Akib S, Khan MTR, Shirazi SM (2014) Experimental study on tsunami risk reduction on coastal building fronted by sea wall. *Sci World J*. <https://doi.org/10.1155/2014/729357>
- Ritter A (1892) Fortpflanzung der wasserwellen. *Vereine Deutscher Ingenieure Zeitschrift* 36(33):947–954
- Robertson IN, Paczkowski K, Riggs HR, Mohamed A (2011) Tsunami bore forces on walls. In: ASME 2011 30th International conference on ocean, offshore and arctic engineering, Rotterdam, The Netherlands, pp 395–403
- Robertson IN, Paczkowski K, Riggs HR, Mohamed A (2013) Experimental investigation of tsunami bore forces on vertical walls. *J Offshore Mech Arct Eng* 135(2):021601-021601-8
- Ryu Y, Chang K-A, Lim HJ (2005) Use of bubble image velocimetry for measurement of plunging wave impinging on structure and associated greenwater. *Meas Sci Technol* 16(10):1945–1953
- Ryu Y, Chang K-A, Mercier R (2007a) Runup and green water velocities due to breaking wave impinging and overtopping. *Exp Fluids* 43(4):555–567
- Ryu Y, Chang K-A, Mercier R (2007b) Application of dam-break flow to green water prediction. *Appl Ocean Res* 29(3):128–136
- Shafiei S, Melville BW, Shamseldin AY (2016) Experimental investigation of tsunami bore impact force and pressure on a square prism. *Coast Eng* 110:1–16
- Shimozono T et al (2012) Propagation and inundation characteristics of the 2011 Tohoku Tsunami on the central Sanriku coast. *Coast Eng J* 54(01):1250004
- Smith L (2014) Experimental investigation of breaking waves on beaches. Master Thesis, Faculty of Mathematics and Natural Sciences, University of Oslo, Norway
- Song YK, Chang K-A, Ryu Y, Kwon SH (2013) Experimental study on flow kinematics and impact pressure in liquid sloshing. *Exp Fluids* 54(9):1–20
- Song YK, Chang K-A, Ariyaratne K, Mercier R (2015) Surface velocity and impact pressure of green water flow on a fixed model structure in a large wave basin. *Ocean Eng* 104:40–51
- St-Germain P, Nistor I, Townsend R, Shibayama T (2014) Smoothed-particle hydrodynamics numerical modeling of structures impacted by tsunami bores. *J Waterw Port C* 140(1):66–81
- Takahashi S et al (2011) Urgent survey for 2011 great east japan earthquake and tsunami disaster in ports and coasts—part I (tsunami), Port and Airport Research Institute (PARI), Yokosuka, Japan
- Thusyanithan NI, Madabhushi SPG (2008) Tsunami wave loading on coastal houses: a model approach. *P I Civil Eng Civ Eng* 161(2):77–86
- Tomita T, Imamura F, Arikawa T, Yasuda T, Kawata Y (2006) Damage caused by the 2004 Indian Ocean Tsunami on the southwestern coast of Sri Lanka. *Coast Eng J* 48(02):99–116

- Vidic-Perunovic J, Lee L, Glomnes EB, Mercier RS, Head WJ (2017) Ultra-deepwater production system: model test study of cylindrical FPSO in GoM hurricane conditions. In: Offshore technology conference, vol. 22
- Wüthrich D, Pfister M, De Cesare G, Schleiss AJ (2016) Velocity profile measurements in bore waves. In: 10th International symposium on ultrasonic doppler methods for fluid mechanics and fluid engineering, Tokyo, Japan, pp 137–140
- Yeh HH (1991) Tsunami bore runup. *Nat Hazards* 4(2):209–220
- Yeh H (2007) Design tsunami forces for onshore structures. *J Disaster Res* 2(6):531–536

Publisher's Note Springer Nature remains neutral with regard to jurisdictional claims in published maps and institutional affiliations.

Affiliations

Wei-Liang Chuang^{1,2} · **Kuang-An Chang**^{1,3}  · **James Kaihatu**¹ · **Rodrigo Cienfuegos**^{4,5} · **Cyril Mokrani**⁴

¹ Zachry Department of Civil and Environmental Engineering, Texas A&M University, College Station, TX, USA

² Present Address: Department of Marine Environment and Engineering, National Sun Yat-sen University, Kaohsiung, Taiwan

³ Department of Ocean Engineering, Texas A&M University, College Station, TX, USA

⁴ Departamento de Ingeniería Hidráulica y Ambiental, Pontificia Universidad Católica de Chile, Santiago, Chile

⁵ Centro de Investigación para la Gestión Integrada del Riesgo de Desastres (CIGIDEN), ANID/Fondap/15110017, Vicuña Mackena 4860, Santiago, Chile